A&A 430, 549–560 (2005)
DOI: 10.1051/0004-6361:20040437

Astronomy & Astrophysics

The interstellar $C^{18}O/C^{17}O$ ratio in the solar neighbourhood: The ρ Ophiuchus cloud⋆

J. G. A. Wouterloot[1,2], J. Brand[3], and C. Henkel[4]

[1] Joint Astronomy Centre, 660 N. A'ohoku Place, University Park, 96720 Hilo, Hawaii, USA
e-mail: j.wouterloot@jach.hawaii.edu
[2] Radioastronomisches Institut, Univ. Bonn, Auf dem Hügel 71, 53121 Bonn, Germany
[3] Istituto di Radioastronomia, CNR, via Gobetti 101, 40129 Bologna, Italy
[4] Max-Planck-Institut für Radioastronomie, Auf dem Hügel 69, 53121 Bonn, Germany

Received 13 March 2004 / Accepted 15 September 2004

Abstract. Observations of up to ten carbon monoxide (CO and isotopomers) transitions are presented to study the interstellar $C^{18}O/C^{17}O$ ratio towards 21 positions in the nearby ($d \sim 140$ pc) low-mass star forming cloud ρ Oph. A map of the $C^{18}O$ $J = 1$–0 distribution of parts of the cloud is also shown. An average $^{12}C^{18}O/^{12}C^{17}O$ isotopomeric ratio of 4.11 ± 0.14, reflecting the $^{18}O/^{17}O$ isotope ratio, is derived from Large Velocity Gradient (LVG) calculations. From LTE column densities we derive a ratio of 4.17 ± 0.26. These calculations also show that the kinetic temperature decreases from about 30 K in the cloud envelope to about 10 K in the cloud cores. This decrease is accompanied by an increase of the average molecular hydrogen density from 10^4 cm^{-3} to $\gtrsim 10^5$ cm^{-3}. Towards some lines of sight $C^{18}O$ optical depths reach values of order unity.

Key words. ISM: abundances – ISM: clouds – ISM: molecules – Galaxy: abundances – radio lines: ISM – ISM: individual objects: rho Oph

1. Introduction

Abundance ratios of interstellar isotopomers are a powerful tool to study the chemical evolution of the Galaxy. One such ratio is that of the rare species of oxygen, ^{18}O and ^{17}O, as measured from the isotopomers of CO. For the galactic disk and -center region, Penzias (1981) reported average $^{18}O/^{17}O$ ratios of 3.65 ± 0.15 and 3.5 ± 0.2, respectively. He also found that the $^{18}O/^{17}O$ ratio, determined from the integrated line intensity ratios $\int T[^{12}C^{18}O(1-0)]dv / \int T[^{12}C^{17}O(1-0)]dv$, shows no significant gradient with galactocentric distance R out to 10 kpc (solar circle: $R_0 = 8.5$ kpc): the $^{18}O/^{17}O$ ratios of the galactic disk and -center are, within the limits of observational accuracy, identical. Models of the chemical evolution of the Galaxy by Prantzos et al. (1996) suggest that after a few Gyr the ratios in the Galaxy should be independent of galactocentric radius. There is, however, a discrepancy between the interstellar medium (ISM) values and the much higher (5.5; Anders & Grevesse 1989) solar system one. Heikkilä et al. (1998) obtain a low value of 1.6 ± 0.3 in the LMC, while in the nuclear starbursts NGC 253 and NGC 4945 $^{18}O/^{17}O \sim 6.5$ (Harrison et al. 1999; Wang et al. 2004). These results suggest that the $^{18}O/^{17}O$ ratio depends on metallicity.

The sources observed by Penzias are located in a limited range of galactocentric radius (and therefore metal abundance), and we (Wouterloot et al., in preparation) have reobserved these sources with higher angular resolution and have extended our study to sources out to $R = 16$ kpc. While Penzias (1981) only observed the $J = 1$–0 transition, our observations also include the $J = 2$–1 rotational lines. The goal of the present paper is to study in detail excitation and opacity effects that could affect the measured $^{18}O/^{17}O$ ratios and radial gradients on small scales. These effects are usually either ignored or physical parameters are derived by assuming a fixed $^{18}O/^{17}O$ ratio, so that a more careful study is desirable.

We have chosen the ρ Oph cloud ($d \sim 140$ pc) because of the large range in column densities found therein, and because it is in the solar neighbourhood so that a high linear resolution can be attained towards this object. Twenty one positions were selected for observations from a $C^{18}O(1–0)$ map of Wilking & Lada (1983) to have a range of $C^{18}O(1–0)$ intensities. Towards the positions with the strongest lines we not only observed the $J = 1$–0 and 2–1 lines of four isotopomers ($^{12}C^{16}O$, hereafter ^{12}CO; $^{13}C^{16}O$, hereafter ^{13}CO; $^{12}C^{18}O$, hereafter $C^{18}O$; $^{12}C^{17}O$, hereafter $C^{17}O$), but we also measured the $J = 3$–2 lines of $C^{18}O$ and $C^{17}O$.

⋆ Based on observations collected with the Swedish/ESO Submillimeter Telescope (SEST) at the European Southern Observatory, Chile (ESO 62.I-0752). All spectra (some of which are shown in Fig. 3) are available in electronic form at the CDS via anonymous ftp to cdsarc.u-strasbg.fr (130.79.128.5) or via http://cdsweb.u-strasbg.fr/cgi-bin/qcat?J/A+A/430/549

2. Observations

2.1. SEST observations

Between September 19 and October 5, 1987 we used the 15-m Swedish-ESO Submillimeter Telescope (SEST) to map $C^{18}O(1–0)$ towards a part of the ρ Oph cloud. We employed a Schottky receiver in combination with an acousto-optical spectrometer (AOS) which had a channel separation of about 43 kHz (0.12 km s^{-1}). All observations were made using frequency switching. The spectra were folded and subsequently resampled to a channel width of 0.24 km s^{-1}. The rms of the resampled data is typically 0.14 K (T_A^*). A $15' \times 15'$ region was observed with a 40″ (in part of the map 20″) raster (the beam size of the SEST at 110 GHz is about 47″). The mapped region contains the cloud cores ρOph B1, ρOph C, ρOph E, and ρOph F, as defined from DCO^+ maps by Loren et al. (1990).

Between January 26 and 31, 1999 we used two SIS receivers at the SEST to observe ^{12}CO, ^{13}CO, $C^{18}O$, and $C^{17}O$ $J = 1–0$ and 2–1 towards 21 positions in the ρ Oph cloud. The observed transitions and frequencies are given in Cols. 1 and 2 of Table 1. Column 3 gives the beam size and Cols. 4 and 5 the main beam- and moon efficiencies of the telescope used (Col. 6). Most intensities in this paper are on the T_A^* scale because then uncertain corrections to T_R^* or T_{mb} do not affect the discussed ratios. In some places, i.e. when comparing lines from different rotational transitions, the use of a different scale (main beam brightness temperature, T_{mb}, or the average of T_A^* and T_{mb}) was unavoidable. This is then mentioned explicitly. The pointing accuracy was about 5″.

The observed positions were selected from the $C^{18}O$ map of Wilking & Lada (1983), and span a large range in $C^{18}O$ intensity and hence in A_v; they are listed in Table 2, in order of decreasing intensity (as estimated from the Wilking & Lada map). Given are a reference number in Col. 1; the position in equatorial coordinates in Cols. 2 and 3; the offset positions with respect to $\alpha(1950) = 16^h24^m10^s$, $\delta(1950) = -24°23'$ (this is the average of the H_2CO (Martin-Pintado et al. 1983) and NH_3 (Zeng et al. 1984) positions determined for core B1 with the 100-m telescope at Effelsberg)[$\alpha(2000) = 16^h27^m11.6^s$, $\delta(2000) = -24°29'42''$], and the rms in the observed transitions in Cols. 6 to 15.

Towards all positions (1 to 21) we observed each of the four isotopomers simultaneously in the $J = 1–0$ and 2–1 transitions. The observations were made using frequency switching and we used the high resolution spectrometer (AOS channel-spacing about 43 kHz) split into two equal parts. Integration times were chosen to obtain similar signal to noise ratios in the $C^{17}O$ and $C^{18}O$ spectra in order to accurately derive the line ratios. In addition to the single positions we made small (3×3) maps centered on the selected 21 positions on a 20″ raster in $C^{18}O$ ($J = 2–1$) to see whether the positions are located in regions with large gradients where pointing errors can influence the observed line ratios, and to be able to convolve the $J = 2–1$ data to the $J = 1–0$ angular resolution.

2.2. JCMT observations

On July 14, 2001, we observed $C^{17}O(3–2)$ towards eight of the 21 positions with the 15-m James Clerk Maxwell Telescope (JCMT) using frequency switching. The velocity resolution of the autocorrelation spectrometer was 0.14 km s^{-1} and the rms noise level ranged from 0.07 to 0.14 K, depending on the line intensity (we tried to reach similar signal-to-noise ratios at all positions).

On February 28, 2002 we observed in the same way $C^{18}O(3–2)$ towards six of the positions previously observed in $C^{17}O(3–2)$. The rms listed in Cols. 8 and 11 of Table 2 was 0.14 to 0.33 K.

Table 1. Observed transitions.

Molecule	Frequency (MHz)	Beam	η_{mb}	η_{moon}	Tel.
$^{12}C^{18}O(1–0)$	109 782.160	47″	0.7	0.9	SEST
$^{13}C^{16}O(1–0)$	110 201.353	47″	0.7	0.9	SEST
$^{12}C^{17}O(1–0)$	112 358.988	46″	0.7	0.9	SEST
$^{12}C^{16}O(1–0)$	115 271.204	45″	0.7	0.9	SEST
$^{12}C^{18}O(2–1)$	219 560.319	24″	0.5	0.9	SEST
$^{13}C^{16}O(2–1)$	220 398.686	24″	0.5	0.9	SEST
$^{12}C^{17}O(2–1)$	224 714.368	24″	0.5	0.9	SEST
$^{12}C^{16}O(2–1)$	230 537.990	23″	0.5	0.9	SEST
$^{12}C^{18}O(3–2)$	329 330.545	14″	0.6	0.9	JCMT
$^{12}C^{17}O(3–2)$	337 061.130	14″	0.6	0.9	JCMT

3. Results

The $C^{18}O(1–0)$ distribution in the mapped region is shown in Fig. 1. The map includes the cloud cores ρOph B1, ρOph C, ρOph E, and ρOph F (see e.g. the 1.3 mm continuum map in Fig. 1 of Motte et al. (1998) which indicates the locations of the cores A, B1, B2, C, D, E, and F). These cores were originally defined in DCO^+ maps by Loren et al. (1990). We show the emission integrated over all velocities (–1 to 8 km s^{-1}) in Fig. 1a and the peak T_A^* distribution in Fig. 1b, respectively. A comparison between the panels (and Gaussian fits to the lines) shows that ρOph B1 and ρOph C (near offsets (0, 0) and (–4, –3) respectively) have relatively narrow lines (about 1.5 km s^{-1}) and a (more) pronounced peak in Fig. 1b, whereas broader (about 2.3 km s^{-1}) lines occur north of ρOph E, near (–1, –8). At the edges of the map, near ρOph F, southwest of ρOph C, and in between ρOph B1 and ρOph C line widths reach values of about 1.0 km s^{-1}. Compared to the lower angular resolution $C^{18}O(1–0)$ map in Fig. 2 of Wilking & Lada (1983; beam size 1.1′ on a 1′ or 2′ raster), the distribution in Fig. 1 shows finer spatial structure. There is also a reasonable correlation between the 1.3 mm continuum in Fig. 1 of Motte et al. (1998) and the $C^{18}O$ distribution. The $C^{18}O$ $J = 1–0$ emission in four 1 km s^{-1}-wide channels is shown in Fig. 2. ρOph C and ρOph E are mainly observed at 4–5 km s^{-1}, whereas ρOph B1 and ρOph F show most emission at 3–4 km s^{-1}.

All spectra measured towards the first three of the twenty-one positions (Table 2) are shown in Fig. 3 (the spectra towards all positions are available as FITS files at CDS). The velocity interval is −8 to +16 km s^{-1}. Most ^{12}CO and some ^{13}CO spectra show self-absorption (a clear minimum in between two peaks in the spectra that is not seen in

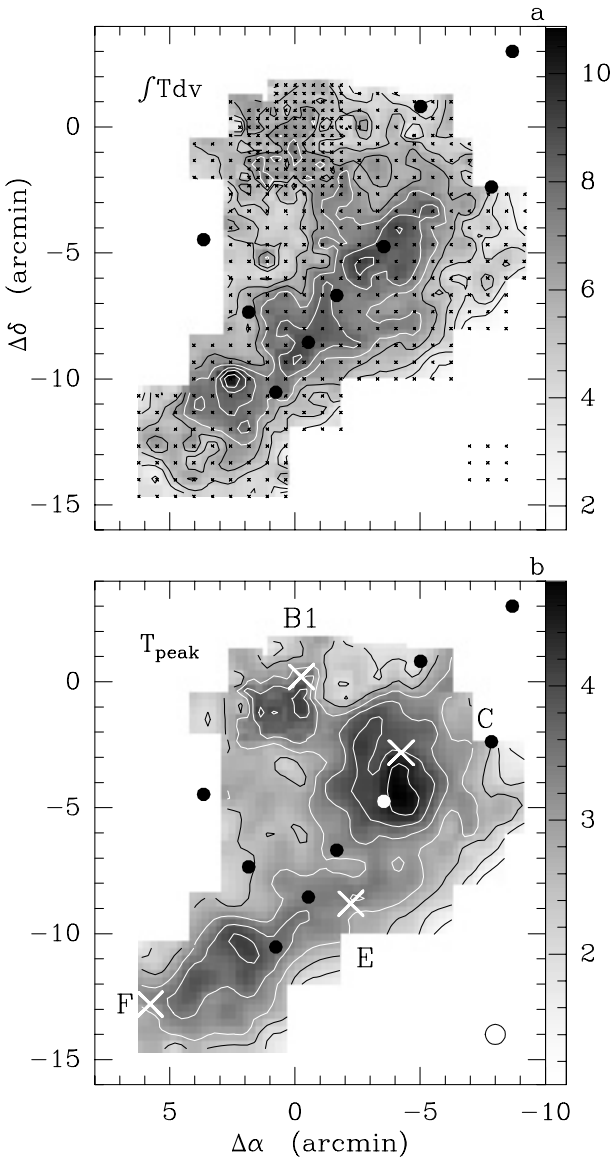

Fig. 1. Distribution of $C^{18}O$(1–0) emission towards the ρ Oph cloud. **a)** Integrated between −1 and +8 km s^{-1}. Contour levels are 2 to 10 K km s^{-1} in steps of 1 K km s^{-1}. Small crosses indicate the observed positions. Offsets are with respect to $\alpha(1950) = 16^h24^m10^s$, $\delta(1950) = -24°23'$. The filled circles are those of the 21 positions (see Table 2) that were also observed in other isotopomers and that are located within or very near the mapped region. **b)** Peak T_A^* in the same velocity interval. Contour levels are 0.5 to 4.5 K in steps of 0.5 K. The open circle indicates the angular resolution of the SEST. The crosses indicate in order of decreasing declination the DCO^+ cores B1, C, E, and F (Loren et al. 1990).

the lines of the rarer CO isotopomers). If flat-topped spectra are also considered as an indication for self-absorption, this phenomenon occurs at even more positions. The numbers in the boxes of the $C^{18}O$(2–1) profiles show the values of $\int T_A^*[C^{18}O(2-1)]dv$ for the 20″-spaced nine-point map around each position. Some positions show significant (10 to 15%) intensity gradients where pointing differences between $C^{18}O$ and $C^{17}O$ (which were not observed simultaneously) could influence the derived line ratios. Equivalent line

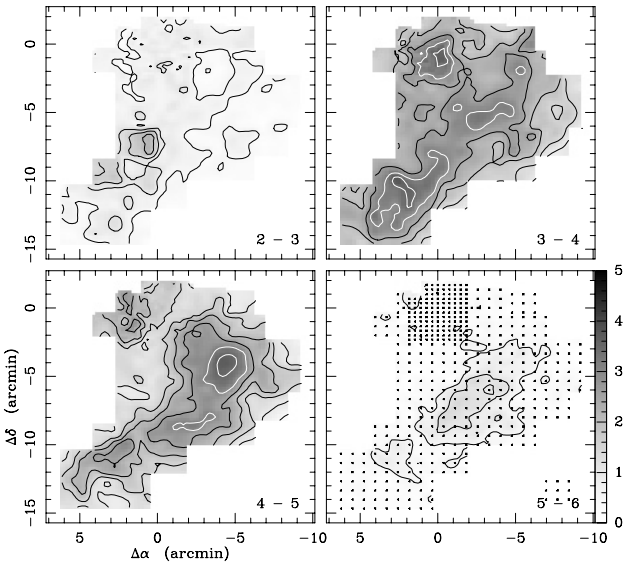

Fig. 2. $C^{18}O$(1–0) distribution in four velocity intervals (given in the lower right hand corner of each panel). Contour levels are 0.5 to 4.5 K km s^{-1} in steps of 0.5 K km s^{-1}.

widths ($\int T_A^* dv/1.06T_A^*$[peak]) for $C^{18}O$(1–0) range between 0.84 km s^{-1} (pos. 14) and 1.91 km s^{-1} (pos. 8). At many positions the $C^{18}O$ and $C^{17}O$ line profiles show the presence of several velocity components, which are more pronounced in ^{13}CO and ^{12}CO (but at slightly different velocities, probably due to self-absorption and saturation in the more abundant isotopomers). Two of these velocity components are visible (at 3–4 and 4–5 km s^{-1}) in the $C^{18}O$(1–0) channel maps of Fig. 2. The $C^{17}O$ spectra also show hyperfine structure (see e.g. Lovas & Krupenie 1974).

4. Isotopomeric ratios

4.1. Isotopomeric ratios derived from line intensities

Integrated line intensities over the velocity interval −1.5 to 8 km s^{-1} (i.e. over all velocity components) and their ratios at the measured 21 positions are listed in Table 3 for $C^{17}O$, $C^{18}O$, and ^{13}CO. For each position the first line gives the intensities (Cols. 2 to 9) and ratios (Cols. 10 to 14) and the second line the uncertainty therein, obtained from the rms in the baseline. We note that while we obtained the positions from the $C^{18}O$(1–0) map of Wilking & Lada (1983) and ordered them according to an expected decrease in integrated intensity, we see this in our results, but there is significant scatter. This is likely caused by a lower angular resolution and undersampling in the Wilking & Lada map, compared to our data. The selected positions cover a large range in $C^{18}O$(1–0) integrated intensity (from 0.98 to 8.59 K km s^{-1}) (or $A_v \approx 10$ to 200 mag (using column densities in Table 4 and Frerking et al. 1982)), as intended.

The resulting $C^{18}O/C^{17}O$ and $^{13}CO/C^{18}O$ integrated line intensity ratios for the (1–0) and (2–1) transitions as a function of $\int T_A^*[C^{17}O(1-0)]dv$ (the most optically thin transition) are shown in Figs. 4a–d. Here (not in Table 3, following Penzias 1981) we corrected the ratios for the difference in frequency, which amounts for $C^{18}O/C^{17}O$ to a factor 1.047

Table 2. Observed sources and rms values (K on a T_A^* scale) for individual transitions.

Pos.	α(1950)	δ(1950)	Offset[a]		rms $C^{17}O$			rms $C^{18}O$			rms ^{13}CO		rms ^{12}CO	
	h m s	° ′ ″	′		1–0	2–1	3–2	1–0	2–1	3–2	1–0	2–1	1–0	2–1
1	16 23 54.0	–24 27 45	–3.55	–4.75	0.023	0.029	0.085	0.050	0.070	0.14	0.12	0.20	0.20	0.23
2	16 23 11.6	–24 14 20	–13.20	8.27	0.025	0.042	0.140	0.068	0.091	0.21	0.07	0.14	0.27	0.26
3	16 24 02.1	–24 31 33	–0.53	–8.55	0.018	0.032	0.071	0.070	0.066	0.19	0.15	0.20	0.30	0.30
4	16 24 02.7	–24 29 41	–1.67	–6.68	0.019	0.025	0.081	0.053	0.078	0.20	0.15	0.22	0.27	0.26
5	16 23 28.6	–24 16 34	–9.43	6.60	0.017	0.031	0.076	0.052	0.077	0.33	0.13	0.20	0.30	0.30
6	16 24 13.4	–24 33 32	0.77	–10.53	0.026	0.028	0.086	0.060	0.087	0.28	0.17	0.20	0.30	0.33
7	16 23 31.9	–24 20 00	–8.68	3.00	0.016	0.029	0.145	0.058	0.077		0.14	0.21	0.34	0.30
8	16 24 18.1	–24 30 21	1.85	–7.35	0.013	0.020	0.103	0.045	0.051		0.12	0.19	0.35	0.33
9	16 23 11.2	–24 13 30	–13.38	9.50	0.020	0.029		0.072	0.074		0.12	0.20	0.34	0.30
10	16 23 48.0	–24 22 11	–5.02	0.82	0.019	0.031		0.104	0.063		0.14	0.19	0.39	0.34
11	16 24 26.0	–24 27 28	3.65	–4.47	0.023	0.033		0.079	0.059		0.15	0.18	0.33	0.28
12	16 23 33.8	–24 10 48	–8.25	12.20	0.018	0.025		0.071	0.059		0.14	0.22	0.36	0.33
13	16 23 35.5	–24 25 23	–7.85	–2.38	0.012	0.020		0.067	0.060		0.13	0.24	0.38	0.33
14	16 23 50.0	–24 18 20	–4.55	4.67	0.016	0.026		0.071	0.049		0.16	0.20	0.39	0.36
15	16 23 18.3	–24 18 14	–11.77	4.77	0.012	0.017		0.076	0.051		0.16	0.23	0.36	0.34
16	16 23 20.5	–24 23 06	–11.27	–0.10	0.0072	0.014		0.031	0.030		0.15	0.21	0.38	0.35
17	16 24 20.9	–24 15 23	2.48	7.62	0.011	0.016		0.057	0.042		0.13	0.22	0.33	0.34
18	16 23 12.8	–24 09 16	–13.02	13.73	0.011	0.012		0.051	0.041		0.13	0.22	0.32	0.28
19	16 23 05.8	–24 23 06	–14.62	–0.10	0.010	0.019		0.038	0.032		0.16	0.21	0.35	0.32
20	16 24 33.4	–24 15 23	5.33	7.62	0.0066	0.010		0.034	0.037		0.13	0.19	0.32	0.38
21	16 23 25.6	–24 07 07	–10.12	15.88	0.010	0.017		0.042	0.050		0.14	0.23	0.28	0.30

[a] With respect to $\alpha(1950) = 16^h24^m10^s$, $\delta(1950) = -24°23'$

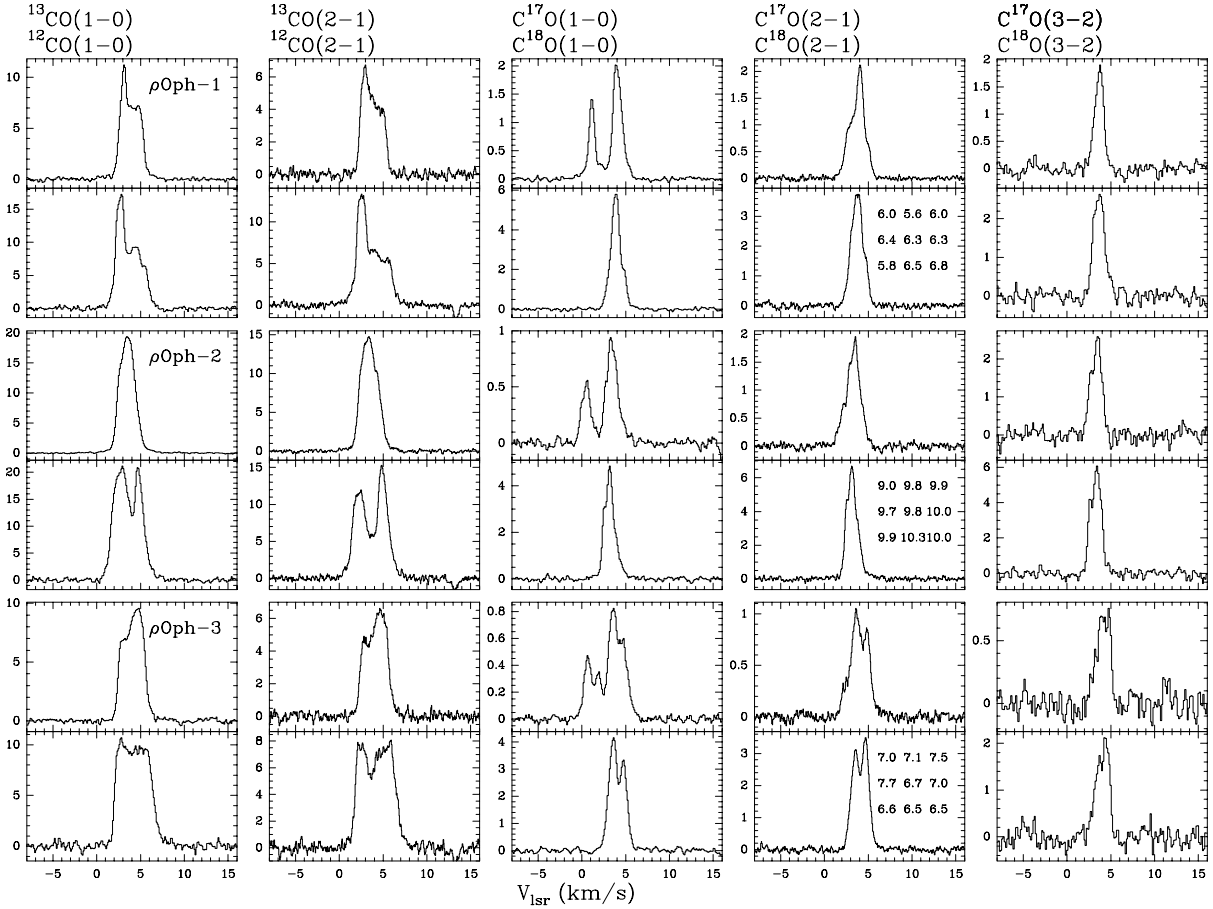

Fig. 3. ^{12}CO, ^{13}CO, $C^{18}O$ and $C^{17}O$ spectra towards the first three of the selected positions given in Table 2. Numbers in the $C^{18}O$(2–1) panels indicate integrated line intensities in K km s^{-1} on a 20″ raster centered at the respective position. The complete set of spectra can be obtained in FITS format at CDS.

Table 3. Observed $C^{17}O$, $C^{18}O$, and ^{13}CO (1–0), (2–1), and (3–2) integrated line intensities and line ratios (i.e. not corrected for the frequency difference). For each position the second line gives the formal errors not including calibration uncertainties.

Pos.	$C^{17}O$			$C^{18}O$			^{13}CO		$\frac{C^{18}O}{C^{17}O}$	$\frac{C^{18}O}{C^{17}O}$	$\frac{C^{18}O}{C^{17}O}$	$\frac{^{13}CO}{C^{18}O}$	$\frac{^{13}CO}{C^{18}O}$
	(1–0)	(2–1)	(3–2)	(1–0)	(2–1)	(3–2)	(1–0)	(2–1)	(1–0)	(2–1)	(3–2)	(1–0)	(2–1)
					K km s^{-1}								
1	4.12	3.79	2.03	8.59	6.60	4.06	24.45	15.46	2.08	1.74	2.00	2.85	2.34
	0.02	0.02	0.10	0.05	0.05	0.16	0.12	0.15	0.02	0.02	0.12	0.02	0.03
2	2.25	3.52	3.52	6.82	10.07	8.42	43.07	35.38	3.03	2.86	2.39	6.31	3.51
	0.03	0.03	0.16	0.07	0.07	0.24	0.08	0.10	0.05	0.03	0.13	0.07	0.03
3	2.50	2.43	1.22	8.33	7.17	3.13	27.03	19.12	3.33	2.95	2.57	3.24	2.66
	0.02	0.02	0.08	0.07	0.05	0.22	0.15	0.15	0.04	0.03	0.25	0.03	0.03
4	2.62	2.29	1.49	7.52	6.62	3.65	25.33	18.31	2.87	2.89	2.45	3.37	2.77
	0.02	0.02	0.09	0.05	0.06	0.23	0.16	0.16	0.03	0.03	0.22	0.03	0.03
5	1.27	2.69	3.38	4.27	6.74	8.48	34.31	28.68	3.36	2.50	2.51	8.03	4.26
	0.02	0.02	0.09	0.05	0.06	0.38	0.14	0.15	0.06	0.03	0.13	0.11	0.04
6	2.00	2.06	0.95	7.02	6.00	3.21	22.31	16.41	3.51	2.91	3.37	3.18	2.73
	0.03	0.02	0.10	0.06	0.06	0.33	0.18	0.15	0.06	0.04	0.49	0.04	0.04
7	1.97	3.71	4.85	6.31	8.84		33.63	23.46	3.20	2.38		5.33	2.65
	0.02	0.02	0.17	0.06	0.06		0.14	0.15	0.04	0.02		0.06	0.02
8	1.47	1.37	0.57	5.20	4.84		24.02	15.08	3.55	3.53		4.61	3.12
	0.01	0.01	0.12	0.05	0.04		0.13	0.14	0.05	0.05		0.05	0.04
9	2.04	3.44		7.79	10.85		40.61	29.41	3.82	3.15		5.21	2.71
	0.02	0.02		0.08	0.05		0.12	0.15	0.05	0.02		0.05	0.02
10	1.41	1.63		2.97	4.27		21.81	14.73	2.10	2.62		7.35	3.45
	0.02	0.02		0.11	0.05		0.14	0.14	0.08	0.05		0.27	0.05
11	1.25	1.17		4.53	3.80		20.52	13.59	3.62	3.24		4.53	3.58
	0.02	0.02		0.08	0.04		0.15	0.13	0.09	0.08		0.09	0.05
12	1.20	2.36		4.32	5.47		24.53	16.41	3.60	2.32		5.69	3.00
	0.02	0.02		0.07	0.04		0.14	0.16	0.08	0.03		0.10	0.04
13	0.83	1.38		2.40	3.47		25.52	16.69	2.88	2.52		10.63	4.80
	0.01	0.01		0.07	0.04		0.13	0.18	0.09	0.04		0.31	0.08
14	0.95	1.35		2.87	3.30		16.25	14.59	3.00	2.45		5.66	4.43
	0.02	0.02		0.07	0.04		0.17	0.15	0.09	0.04		0.16	0.07
15	1.07	2.06		3.71	6.40		37.64	33.15	3.47	3.11		10.14	5.18
	0.01	0.01		0.08	0.04		0.17	0.17	0.08	0.03		0.22	0.04
16	0.33	0.59		1.11	1.69		19.45	15.78	3.36	2.86		17.55	9.35
	0.01	0.01		0.03	0.02		0.16	0.15	0.12	0.06		0.53	0.15
17	0.65	0.67		2.36	2.56		16.94	11.33	3.65	3.80		7.17	4.43
	0.01	0.01		0.06	0.03		0.13	0.16	0.11	0.08		0.19	0.08
18	0.55	1.05		1.94	3.32		24.13	17.47	3.55	3.15		12.46	5.27
	0.01	0.01		0.05	0.03		0.13	0.16	0.12	0.04		0.35	0.07
19	0.32	0.67		0.98	1.62		18.85	15.80	3.08	2.43		19.20	9.77
	0.01	0.01		0.04	0.02		0.16	0.15	0.16	0.06		0.80	0.17
20	0.37	0.44		1.56	1.78		17.10	11.87	4.20	4.07		10.95	6.65
	0.01	0.01		0.03	0.03		0.14	0.14	0.12	0.09		0.26	0.13
21	0.40	0.88		1.67	2.29		17.92	12.85	4.16	2.61		10.71	5.61
	0.01	0.01		0.04	0.04		0.15	0.17	0.15	0.06		0.30	0.12

($C^{18}O/C^{17}O$(corrected) = $(\nu_{17}/\nu_{18})^2$ $C^{18}O/C^{17}O$(observed), see Linke et al. 1977), but not for optical depth and excitation effects. Therefore, if these effects are negligible, the corrected ratios should be equivalent to those of the column densities. Formal errors derived from the uncertainties in the line areas (see Table 3) are small with respect to the errors introduced by the calibration uncertainties. The latter may amount to 7% causing an error in the ratios of 10%. The 3×3 $C^{18}O$(2–1) maps around the observed positions (see Fig. 3) show that over an angular scale of 20″ the change in integrated intensity is typically 10% or less. This implies that pointing errors of 5″ cause errors of a few percent in the observed line intensity ratios. In Fig. 4b we also show (as filled circles) the $C^{18}O/C^{17}O$ ratios derived from the JCMT J = 3–2 observations. These agree well with the J = 2–1 and J = 1–0 results. For comparison we also show in Fig. 4a the average result from Penzias (1981) for the galactic disk as a dashed line, and the value towards our pos. 1 derived by Bensch et al. (2001) from $^{13}C^{18}O$ and $^{13}C^{17}O$(1–0) observations as a dotted line.

At pos. 1, where integrated $C^{17}O$ line intensities and CO column densities are highest, the observed $C^{18}O/C^{17}O$ ratios are significantly lower than towards the other positions (see

Table 4. Derived parameters using average beam efficiencies.

Pos	Ratio $C^{18}O/C^{17}O$		T_{ex}	τ $C^{17}O$	N	T_{ex} $C^{18}O$	T_{ex} $^{12}CO(1–0)$	Ratio	T_{kin}	log[$n(H_2)$]	χ^2
	fcorr	N ratio	K	(tot)	cm^{-2}	K	K	$C^{18}O/C^{17}O$	K LVG	cm^{-3}	
	$J = 1–0$										
	$J = 2–1$										
1	2.18	–	8.0	1.09	7.2×10^{15}	6.9	22.9	4.5	9.4	5.19	4.5
	1.82	–		1.45	7.4×10^{15}						
2	3.17	4.22	13.6	0.19	3.0×10^{15}	12.4	27.3	4.0	17.8	4.89	6.8
	3.00	–		0.43	3.1×10^{15}						
3	3.49	–	8.7	0.30	3.1×10^{15}	7.7	15.5	4.25	11.5	4.71	18
	3.09	–		0.47	3.0×10^{15}						
4	3.01	–	7.9	0.43	3.4×10^{15}	7.8	19.3	3.75	11.2	4.71	20
	3.03	–		0.51	3.2×10^{15}						
5	3.52	3.00	24.8	0.05	2.2×10^{15}	14.5	36.3	3.5	23.2	4.71	11
	2.62	3.76		0.15	2.3×10^{15}						
6	3.67	–	8.7	0.28	2.4×10^{15}	7.4	18.3	5.0	10.3	4.77	4.7
	3.05	8.95		0.41	2.4×10^{15}						
7	3.35	4.03	16.1	0.12	2.7×10^{15}	10.9	31.5	3.88	15.4	4.80	2.7
	2.49	3.51		0.33	2.9×10^{15}						
8	3.72	5.30	8.0	0.19	1.7×10^{15}	7.8	16.6	4.5	10.6	4.47	2.9
	3.70	8.56		0.28	1.6×10^{15}						
9	4.00	5.57	13.6	0.14	2.6×10^{15}	10.7	24.9	5.0	14.8	4.83	0.9
	3.30	6.03		0.29	2.7×10^{15}						
10	2.20	2.54	10.3	0.26	1.8×10^{15}	12.7	26.1	3.0	12.2	4.59	14
	2.75	2.91		0.38	1.7×10^{15}						
11	3.78	8.11	8.2	0.23	1.5×10^{15}	7.4	19.2	5.5	9.1	4.71	0.0
	3.40	9.08		0.36	1.4×10^{15}						
12	3.77	3.92	18.4	0.07	1.7×10^{15}	10.3	22.0	4.5	10.3	4.71	14
	2.43	5.88		0.17	1.8×10^{15}						
13	3.01	3.12	14.1	0.08	1.1×10^{15}	11.7	23.0	3.25	11.2	4.41	0.7
	2.64	3.38		0.14	1.0×10^{15}						
14	3.14	4.04	12.1	0.15	1.2×10^{15}	9.6	23.5	4.25	9.7	4.71	0.2
	2.56	4.96		0.25	1.2×10^{15}						
15	3.63	3.51	18.7	0.05	1.6×10^{15}	15.3	25.7	3.88	18.3	4.47	0.5
	3.26	3.98		0.12	1.5×10^{15}						
16	3.52	3.21	17.6	0.03	4.6×10^{14}	13.6	24.1	3.5	11.2	4.11	6.1
	2.99	3.23		0.05	4.4×10^{14}						
17	3.82	4.57	9.3	0.12	7.4×10^{14}	9.5	19.7	4.63	10.8	4.41	4.3
	3.97	5.16		0.19	7.1×10^{14}						
18	3.72	3.49	17.5	0.03	7.6×10^{14}	14.5	21.7	3.75	18.4	4.23	0.5
	3.30	3.77		0.08	7.5×10^{14}						
19	3.22	2.36	29.5	0.01	6.1×10^{14}	17.5	31.3	3.0	32.5	3.87	9.6
	2.55	2.30		0.03	6.1×10^{14}						
20	4.39	4.75	9.5	0.04	4.0×10^{14}	9.0	19.3	4.5	11.2	3.99	0.2
	4.26	4.91		0.07	3.8×10^{14}						
21	4.36	3.38	23.2	0.02	6.6×10^{14}	11.2	19.1	4.25	11.2	4.41	41
	2.74	3.74		0.07	6.5×10^{14}						

Figs. 4a,b). This holds for all three observed rotational transitions. At pos. 10 the $C^{18}O/C^{17}O$ ratio is lower than at other positions (except pos. 1) for J = 1–0 but not for J = 2–1. Omitting pos. 1, the unweighted average of the $C^{18}O/C^{17}O$ integrated intensity ratios (including frequency correction) is 3.53 ± 0.48 (sd; me 0.11) for the (1–0) and 3.06±0.49 (sd; me 0.11) for the (2–1) transition (for average values we derive both the standard deviation (sd) and the error in the mean (me = sd/$\sqrt{N}$), which is the most relevant parameter describing the uncertainty of the average values). For J = 3–2 (positions 2 to 6) we obtain a ratio of 2.78 ± 0.40 (sd; me 0.18); for the same positions the J = 1–0 and 2–1 ratios are 3.37 ± 0.26 (sd; me 0.12) and 2.95 ± 0.18 (sd; me 0.08), respectively, suggesting a decrease of the ratio with J, possibly because of increasing optical depth (see Sect. 4.2.3). At pos. 1 the ratios are 2.18 ± 0.02 (1–0), 1.82 ± 0.02 (2–1), and 2.09 ± 0.12 (3–2).

In Figs. 4c, d $^{13}CO/C^{18}O$ ratios are shown for the (1–0) and (2–1) transitions. This ratio may be strongly affected by ^{13}C fractionation for small column densities (Bally & Langer 1982; Langer et al. 1984), self-shielding (van Dishoeck & Black 1988), and by high ^{13}CO optical depths at large column densities, which explains the decrease from 10 to 20 in

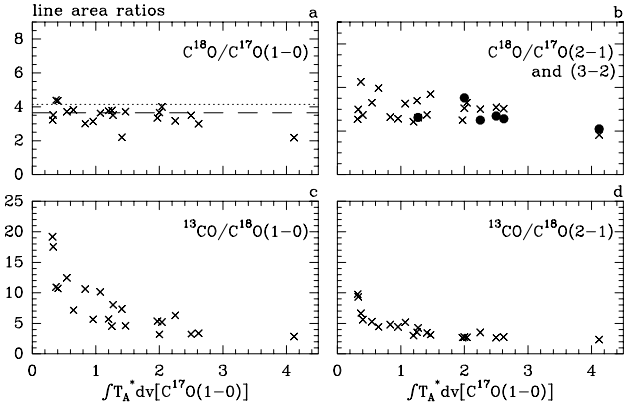

Fig. 4. $C^{18}O/C^{17}O$ and $^{13}CO/C^{18}O$ isotopomeric ratios as a function of $\int T_A^*[C^{17}O(1–0)]dv$ for **a**), **c**) J = 1–0, **b**), **d**) J = 2–1 (crosses) and **b**) J = 3–2 (filled circles). The $C^{18}O/C^{17}O$ and $^{13}CO/C^{18}O$ line area ratios have been corrected for the frequency difference (see Sect. 4.1). The dashed line indicates the ratio found by Penzias (1981) for the galactic disk, and the dotted line denotes the result from Bensch et al. (2001) from $^{13}C^{18}O$ and $^{13}C^{17}O$(1–0).

the outer parts of the ρ Oph cloud to about 3 in the cloud centre. This decline in integrated line intensity ratios is similar to that seen in Barnard 5 (Langer et al. 1989, their Fig. 5), but in ρ Oph $^{13}CO/C^{18}O$ ratios reach even lower values than in Barnard 5. Towards the very outer parts of Barnard 5 where $\int T[^{13}CO(1–0)]dv$ is 1–4 K km s^{-1}, this ratio also decreases. In ρ Oph we do not see this effect, possibly because here the ^{13}CO emission is much stronger towards all observed positions. We note that Zielinsky et al. (2000) could explain increasing $^{13}CO/C^{18}O$ ratios towards the edge of a Photon Dominated Region (PDR) by the presence of few big clumps in the cloud center and many small clumps at the cloud edge.

4.2. Isotopomeric ratios derived from LTE column densities

The isotopomeric ratios are likely to be affected by optical depth effects, which will be strong for CO (most positions show self-absorption), significant for ^{13}CO, and not negligible for $C^{18}O$. For $C^{17}O$ small optical depths are expected towards all observed lines of sight. At pos. 1, which shows the highest $C^{17}O$ column density, the observed integrated intensity ratios for J = 1–0 $C^{18}O/^{13}C^{18}O$ and $C^{17}O/^{13}C^{17}O$ are 35.8 and 68.7, respectively (Bensch et al. 2001), indicating (assuming that the $^{12}C/^{13}C$ ratio is about 70; Wilson & Rood 1994) that the $C^{18}O$ optical depth is about 1.5 whereas the $C^{17}O$ optical depth is small.

Trying to account for optical depth effects, we have derived Local Thermodynamical Equilibrium (LTE) column densities of ^{13}CO, $C^{18}O$, and $C^{17}O$. Below we describe how we calculate excitation temperatures and optical depths.

4.2.1. Excitation temperature

For the calculation of T_{ex}, both the T_A^* and the T_{mb}^* temperatures scales are relevant. The T_{mb}-scale is strictly valid in the extreme case of a source only covering the main beam, while the T_A^*-value applies to the opposite extreme, a very extended source. We have estimated the CO excitation temperatures in two different ways, in each of which we used both T_A^* and T_{mb}^*.

Firstly, we derive excitation temperatures from the peak temperatures of CO(1–0) and CO(2–1) using

$$T_{ex} = 5.532 \left[\ln\left(1 + \frac{5.532}{(T_{10} + 0.819)}\right)\right]^{-1},$$

where T_{10} is the peak $T[^{12}CO(1–0)]$ temperature, or

$$T_{ex} = 11.064 \left[\ln\left(1 + \frac{11.064}{(T_{21} + 0.187)}\right)\right]^{-1},$$

where T_{21} is the peak $T[^{12}CO(2–1)]$ temperature (method 1). This could underestimate the excitation temperature whenever there is self-absorption. The method helps to constrain excitation temperatures, in particular for the outer parts of the cloud.

Secondly we obtain excitation temperatures from the (2–1)/(1–0) ratio of the integrated intensities of $C^{18}O$ and $C^{17}O$, respectively (method 2), assuming that the transitions are optically thin (if this is not the case (mainly for $C^{18}O$) the excitation temperature will be underestimated) and that beam filling effects do not affect the ratio [$C^{17}O$: (2–1)/(1–0) = 4.0 exp(−10.78/T_{ex}); $C^{18}O$: (2–1)/(1–0) = 4.0 exp(−10.54/T_{ex})]. The J = 2–1 $C^{18}O$ and $C^{17}O$ data were convolved to the J = 1–0 resolution using the nine point $C^{18}O$ J = 2–1 maps described in Sect. 2 (see also Fig. 3). The corrections are small (≤5% at most positions, but 16% at pos. 19). In contrast to method 1 that uses optically thick CO lines potentially tracing predominantly cloud envelopes, method 2 is based on tracers that are more representative of the entire molecular column density. A comparison of excitation temperatures derived by methods 1 and 2 can show whether there are temperature gradients in the cloud.

Figures 5a and 5b show the (2–1)/(1–0) $\int T_A^* dv$ ratios for $C^{18}O$ and $C^{17}O$, respectively, as a function of $\int T_A^*[C^{17}O(1–0)]dv$. There is no correlation. In Figs. 5c-f we compare T_{ex} derived from J = 1–0 (Figs. 5c, e) and J = 2–1 (Figs. 5d,f) ^{12}CO T_A^* (Figs. 5c, d) values (this, method 1, should provide upper limits to T_{ex}) with the excitation temperatures of $C^{18}O$ and $C^{17}O$, derived from the $\int T_A^* dv$ (2–1)/(1–0) ratios (method 2). We also show in Figs. 5e, f the excitation temperatures after converting to T_{mb} using the efficiencies in Table 1 (T_{mb}=$T_A^* \eta_{moon}/\eta_{mb}$). The values derived from $T_A^*[^{12}CO]$ range from 14.1 K (J = 1–0) and 13.0 K (J = 2–1) at pos. 3 to 32.7 K (1–0) and 30.9 K (2–1) at pos. 5. These values are for a T_A^* temperature scale. They are even higher for a T_{mb}^* scale: the maximum value is 41 K at pos. 5.

Excitation temperatures derived from $C^{18}O$ and $C^{17}O$ (method 2) are generally lower: 6.3 K (pos. 1) to 14.3 K (pos. 19) ($C^{18}O$) and 7.2 K (pos. 1) to 21.6 K (pos. 19) ($C^{17}O$). Using main beam brightness temperature ratios, the values become larger: 7.9–26.4 K ($C^{18}O$) and 9.3–66.4 K ($C^{17}O$) for the same positions.

The OLS bisector mode was used to derive linear regression coefficients (see Isobe et al. 1990). There is some correlation between the excitation temperatures derived from ^{12}CO

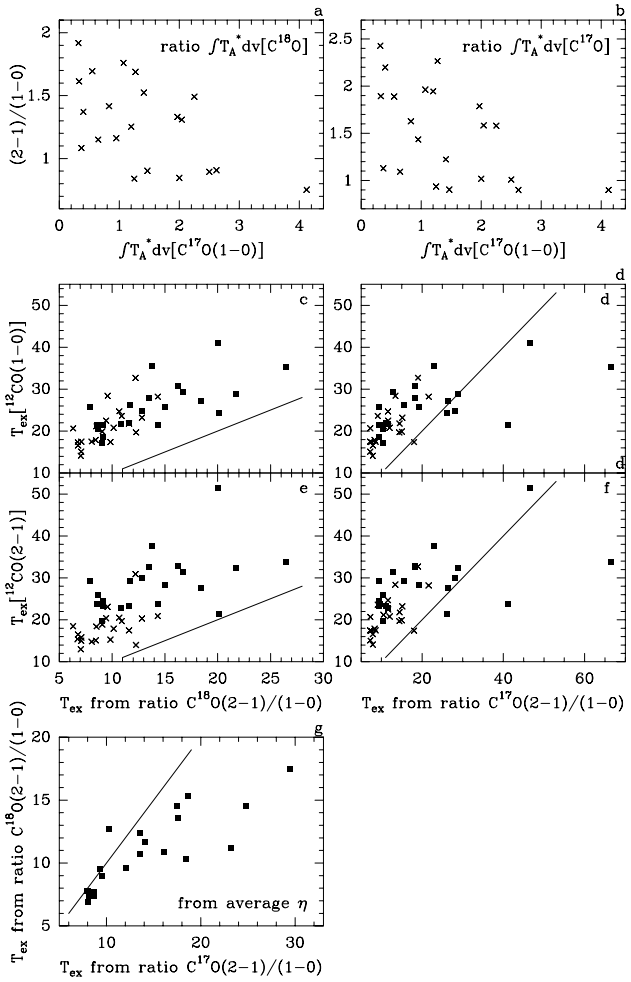

Fig. 5. (2–1)/(1–0) $\int T_A^* dv$ ratios for $C^{18}O$ **a**) and $C^{17}O$ **b**) as a function of $\int T_A^*[C^{17}O(1–0)]dv$. **c**), **d**) $T_{ex}[^{12}CO(1–0)]$ vs. T_{ex} obtained from the ratio (2–1)/(1–0) for $C^{18}O$ **c**) and $C^{17}O$ **d**) using T_A^* (crosses) or T_{mb} (squares). **e**), **f**) The same as in c,d, but for $T_{ex}[^{12}CO(2–1)]$. In **g**) the T_{ex} from $C^{18}O$ and $C^{17}O$ (using the average of Moon and main beam efficiencies) are compared. The drawn lines indicate equal values.

and $C^{18}O$ (the correlation coefficient is 0.70 in Figs. 5c). For $C^{17}O$, the correlation is slightly less well defined (the correlation coefficient is 0.66; Fig. 5d). For $C^{18}O$ the slope is closest to 1 for the T_{mb} ratios (0.93 ± 0.16), while we obtain a slope of 1.97 ± 0.33 for the T_A^* ratios. For $C^{17}O$ this is reversed: for the T_A^* ratios the slope is 1.08 ± 0.15 whereas that for the T_{mb} values it is 0.34 ± 0.08. The higher values for ^{12}CO compared to those from the $C^{18}O$ and $C^{17}O$ (2–1)/(1–0) ratios can be explained by higher kinetic temperatures in the outer parts of the clouds (e.g. Castets et al. 1990) from which the ^{12}CO emission mostly originates.

Because the extent of $C^{18}O$ and $C^{17}O$ clumps is most likely larger than the main beam, but small compared to the size of the Moon we are using in Sects. 4.2.2, 4.2.3, and 4.3 the average of both efficiencies. The resulting T_{ex} for $C^{18}O$ and $C^{17}O$ are compared with each other in Fig. 5g. It shows that T_{ex} is well correlated for both isotopomers, but for $C^{17}O$ it can reach higher values than for $C^{18}O$. There is no correlation between optical depth and T_{ex}, and therefore the lower T_{ex} of $C^{18}O$ cannot be explained by the fact that we did not correct for optically thick J = 2–1 lines.

4.2.2. Optical depth

$C^{18}O$ optical depths are often derived from $C^{18}O$ and $C^{17}O$ data by assuming a certain intrinsic $C^{18}O/C^{17}O$ ratio. However the aim of this paper is to determine this ratio and therefore this method cannot be applied.

We tried to fit the $C^{17}O$ hyperfine components for several positions with small line widths. The optical depth for the main hyperfine component of the J = 1–0 transition had values of less than a few tenths in most cases. The fitting is complicated by the presence of more than one velocity component, such as a broader underlying component (e.g. at pos. 10, which is also seen in $C^{18}O$), or two narrow components (pos. 3, 4, 7). In some cases we could fit line widths and velocities to the corresponding $C^{18}O$(1–0) spectrum and could use those as input values for the fit. Sometimes the fit gave a high optical depth for a weak component, which is not realistic. Limited signal-to-noise ratios prevented better determinations of the optical depth in these components.

We also derived optical depths from the excitation temperatures determined by method 2 using the radiative transfer equation (see e.g. Rohlfs & Wilson 1996, Eq. (14.48)). We find that for excitation temperatures from (2–1)/(1–0) ratios using an average efficiency (as defined in Sect. 4.2.1 and Fig. 5g) the highest total $C^{17}O$(1–0) optical depth (i.e. the resulting peak optical depth if all hyperfine components had the same frequency) is τ_{tot} = 1.09 for pos. 1. This is a little high when considering $^{18}O/^{17}O$ ratios of order 4 (Sect. 5) and the results of Bensch et al. (2001; see Sect. 4.2). It is equivalent to a value for the main hyperfine component of about 0.36. At other positions τ_{tot} ranges from 0.01 to 0.43. For $C^{18}O$(1–0) the optical depth is undeterminable (log of negative number) at pos. 1, 3, 4 and 6 (but see Sect. 4.2). At the other positions it ranges from 0.05 to 2.1.

4.2.3. LTE column density ratios

Using the excitation temperature and optical depth derived above, the column density is calculated from

$$N_{lte} = \frac{3h10^5 1.065}{8\pi^3\mu^2}\frac{\tau\Delta v}{J}Qe^{\frac{E_{J-1}}{kT_{ex}}}\left[1-e^{-h\nu/kT_{ex}}\right]^{-1}$$

with Δv denoting the full width at half maximum intensity of the emission line, where the transition is from level J to level $J-1$; ν is the observed frequency, Q is the partition function (e.g. Rohlfs & Wilson 1996, Eq. (14.50)), and μ the electric dipole moment of the molecule.

Assuming that the structure of the cloud is somewhere in between that of a point source and a very extended source, we used here for all following calculations telescope efficiencies which are the average of the main beam and moon efficiency. Based on the results discussed in the previous sections we decided to adopt for $C^{18}O$ and $C^{17}O$ excitation temperatures and optical depths derived using the respective (2–1)/(1–0) ratios,

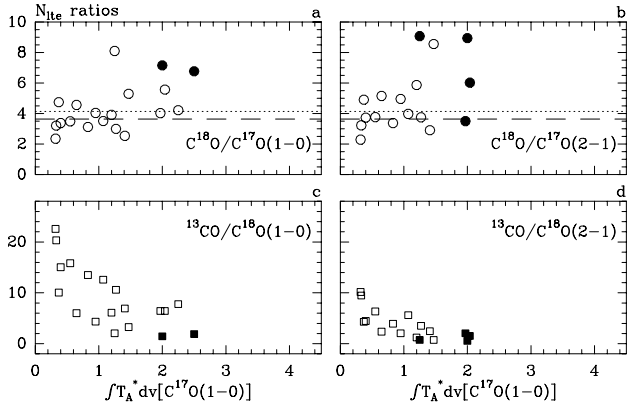

Fig. 6. $C^{18}O/C^{17}O$ **a**), **b**) and $^{13}CO/C^{18}O$ **c**), **d**) isotopomeric ratios as a function of $\int T_A^*[C^{17}O(1–0)]dv$. The ratios were derived from LTE column densities using excitation temperatures derived from the corresponding (2–1)/(1–0) ratios, except for ^{13}CO where we used T_{ex} derived from ^{12}CO. The filled symbols indicate positions where the $C^{17}O$ excitation temperatures were used for the $C^{18}O$ column density. The dashed line indicates the ratio found by Penzias (1981) for the galactic disk, and the dotted line marks the result from Bensch et al. (2001) from $^{13}C^{18}O$ and $^{13}C^{17}O$(1–0).

and for ^{13}CO the commonly adopted excitation temperature from the corresponding ^{12}CO transition. In this way we derive two sets of LTE column density ratios for the $C^{18}O/C^{17}O$ and $^{13}CO/C^{18}O$ ratios, one based on the J = 1–0, the other on the 2–1 data.

The results for the 21 positions are given in Table 4. Col. 1 gives the position, Col. 2 the frequency-corrected $C^{18}O/C^{17}O$ ratio, and Col. 3 the derived column density ratio. The $C^{17}O$ excitation temperature, total optical depth and column density are in Cols. 4 to 6. At each position the first row is for J = 1–0 and the second row for J = 2–1. Cols. 7 and 8 give the excitation temperatures for $C^{18}O$ and ^{12}CO(1–0), respectively.

The unweighted average $N(C^{18}O)/N(C^{17}O)$ LTE ratio for the J = 1–0 transition (see Fig. 6a) is 4.07 ± 1.32 (sd; me 0.32), a higher value than that determined by Penzias (1981), but close to that derived by Bensch et al. (2001) from $^{13}C^{18}O$ and $^{13}C^{17}O$. Omitting here the highest highly uncertain value (above 8.0, at pos. 11) (the τ is close to being undetermined and therefore uncertain), the ratio becomes 3.81±0.23). At four positions (1, 3, 4, 6) the $C^{18}O$ optical depth was undetermined, but for two of those positions (3, 6) a value could be derived using the $C^{17}O$ excitation temperatures. However we did not use these data points to derive the average $N(C^{18}O)/N(C^{17}O)$ ratio. Similarly, for the J = 2–1 transition using the same T_{ex} as above, the $C^{18}O$ optical depths were undetermined at positions 1, 2, 3, 4, 6, 7, 9, and 11, where at positions 1 to 4 also the $C^{17}O$ T_{ex} resulted in undetermined τ's. Ratios derived for this transition are shown in Fig. 6b – the average value without the above mentioned positions is 4.35 ± 0.35. Omitting here the highest value (above 8.0, at pos. 8), the ratio becomes 4.00 ± 0.29.

$N(^{13}CO)/N(C^{18}O)$ ratios are shown in Fig. 6c and d, which were derived from the J = 1–0 and 2–1 data, respectively. One can see that after correction for optical depths the decrease in ratios towards the cloud center remains. This can be explained by real changes in the ratios such as fractionation; modelling them is beyond the scope of this paper.

4.3. Isotopomeric ratios derived from Large Velocity Gradient (LVG) modelling

In order to study the excitation of $C^{18}O$ and $C^{17}O$ in more detail, we also made LVG calculations (e.g. Castor 1970; Scoville & Solomon 1974). Simulating the observed line intensities, one can estimate column densities, H_2 volume densities and kinetic temperatures. The critical point in our LTE approach (Sect. 4.2) is the assumption of a single excitation temperature for all transitions of a given CO isotopomer. The LVG calculations provide a way to estimate in how far differences in derived column densities are accompanied by changes in excitation temperature. In principle, such changes could provide line intensity ratios that do not directly reflect the $^{18}O/^{17}O$ isotope ratio and an LVG code is a suitable tool to investigate such effects.

We used the collision rates from Flower (2001) with an ortho/para H_2 ratio of 3.0. Taking instead a ratio of 0.1 (i.e. almost pure para-H_2) does not significantly alter the results outlined below. Level populations and expected line intensities were calculated for 5 K < T_{kin} < 35 K and 10^3 < $n(H_2)$ < 10^6 cm^{-3}. For $C^{18}O$ we assumed an average abundance of $[C^{18}O]/[H_2]$ = 1.7 10^{-7}, derived by Frerking et al. (1982) for positions in the ρ Oph cloud. In the calculations we used intrinsic ratios of $C^{18}O/C^{17}O$ between 1.5 and 8.0 in steps of 0.25 or 0.5, and adopted a velocity gradient of 5 km s^{-1}pc^{-1}, which is appropriate for the size and line width of the ρ Oph clouds.

Before discussing the results we have to check whether the assumptions used by Frerking et al. (1982) to derive $C^{18}O$ column densities, $N(C^{18}O)$, are the same as used in the present paper. They observed $C^{18}O$(1–0) towards twelve positions and detected eight of them with a maximum T_A of 1.3 K. The positions were selected to have relatively low column densities in order to be able to derive extinctions (A_v < 10 mag, where depletion (see below) is not important). Upper limits to column densities were derived assuming that the $C^{18}O$ excitation temperature equals T_{ex} (^{12}CO) and that all levels are populated. To derive a lower limit to column densities Frerking et al. (1982) assumed the same excitation temperature, but with only the J = 0 and 1 levels populated. The latter is clearly not true because we detected J = 2–1 emission in excess of 1.0 K at positions with $T_A^*[C^{18}O(1–0)]$ < 1.0 K. Then Frerking et al. used the average value of upper and lower limit. Comparing our LTE column densities (Sect. 4.2.3) with values derived using Frerking et al.'s assumptions shows that Frerking et al. underestimate column densities by a factor of 2. Therefore the abundance is too small by that amount.

There is another reason why the assumption of a constant abundance is not necessarily correct. Kramer et al. (1999) found indications of CO depletion by a factor of about 3 in the core of IC 5146 at visual extinction A_v of about 30 mag. IC 5146 is colder than the ρ Oph cloud and Kramer et al. concluded that $C^{18}O$(1–0) and (2–1) are optically thin, which is not the case for all positions in ρ Oph. The depletion starts at visual

extinctions of about 10 mag (Bergin et al. 2002), which would correspond to a $N(C^{18}O)$ of $\approx$2 to 4×10^{15} cm^{-2} (assuming $N(H_2)/A_v$ 0.9×10^{21} cm^{-2}mag^{-1}; Bohlin et al. 1978). This is in the lower range of the column densities at the observed positions (see Table 4). However depletion is not expected to affect isotopomeric ratios and we have done some LVG calculations using a $C^{18}O$ abundance which is a factor of 2 lower than that of Frerking et al. (1982). The results differ only marginally from those obtained with an undepleted abundance and are therefore inconclusive: at all positions the derived H_2 densities are approximately a factor of two larger and the kinetic temperatures are slightly smaller. Because the effects of depletion and the underestimation of column densities by Frerking et al. may balance out, we decided to use the Frerking et al. (1982) abundances in our calculations.

Towards the 21 positions the observed and predicted values of peak $C^{18}O$ temperatures (using averages efficiencies, but also T_A^* and T_{mb} for some calculations) and the $C^{18}O/C^{17}O$ ratios for the J=1–0, 2–1 and 3–2 lines were compared and χ^2 values were calculated using for the temperatures an uncertainty σ of 10% and for the ratios of the three observed rotational transitions a σ of 0.15, 0.15, and 0.20, respectively. The measured temperatures for the J=2–1 and 3–2 transitions were convolved to the J=1–0 beam, as described in Sect. 4.2.1. Columns 9 to 12 of Table 4 give the results of the LVG calculations: $C^{18}O/C^{17}O$ ratio, kinetic temperature, molecular hydrogen density and χ^2, indicating the relative goodness of the solutions between the different positions. Apparently the scatter in isotope ratio is smaller than that obtained with the LTE approach.

The parameters of minimum χ^2 are shown in Fig. 7 (for the assumed $C^{18}O/C^{17}O$ ratio) and Fig. 8 (for T_{kin} and $\log(n(H_2))$). In Fig. 8b the influence of the assumed temperature scale is also shown. The minimum χ^2 values range between 0 (perfect fit) and more than 40 (bad fit; for pos. 21), and do not show a systematically lower value for either temperature scale. Figure 8b shows a general decrease in density and an increase in T_{kin} with decreasing column density (or $\int T_A^*[C^{17}O(1–0)]dv$). LVG modelling assumes that the density is constant along the line of sight, which is probably not true and some lines of sight may have larger density gradients than others in the $C^{17}O$ emitting region.

For all positions except of pos. 1, Fig. 7 shows a clear minimum for some $C^{18}O/C^{17}O$. Ratios ranges from 3.0 to 5.5 with an average value of 4.11±0.65 (sd; me 0.14). Giving a higher weight to positions with lower χ^2 increases the ratio slightly to 4.21. The exception is pos. 1 which has the highest H_2 density, where the χ^2 does not much increase for higher ratios. We did not use ^{13}CO data in these calculations because this isotopomer is too much affected by fractionation which makes it impossible to assume a single fractional abundance. Likewise ^{12}CO data show (much) higher excitation temperatures than the derived kinetic temperatures (see also Figs. 5c–f). This, like the increase in T_{kin} with decreasing column density mentioned above is consistent with kinetic temperatures decreasing towards the cloud interiors from about 20–30 K to 10 K.

We have to check what the LVG calculations predict for T_{ex}, since LTE assumes that they are equal for all levels.

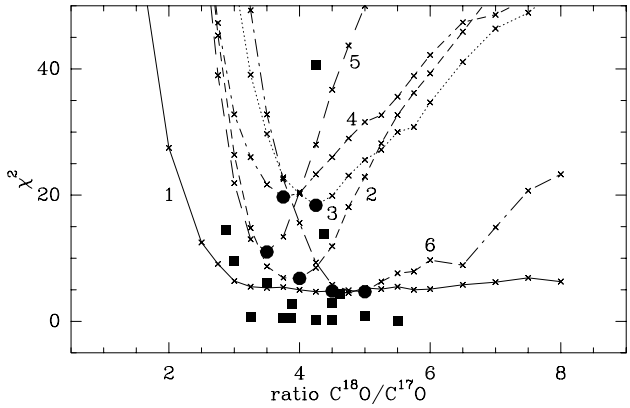

Fig. 7. Results of LVG calculations. Plotted is the derived χ^2 value as a function of the assumed $C^{18}O/C^{17}O$ ratio for the positions 1 to 6. The different positions are distinguished by full drawn, dotted, and dashed lines. The filled symbols indicate the ratio of minimum χ^2 at each of the 21 positions. The circles are for the positions 1–6, where J = 3–2 data exist. The positions associated with the filled squares can be identified in Col. 9 of Table 4. The small crosses mark the $C^{18}O/C^{17}O$ ratio used in the calculations.

Figure 9 shows results of the LVG calculations for an assumed $C^{18}O/C^{17}O$ ratio of 4.0. In Fig. 9a the dotted lines indicate the predicted $T_{ex}(J = 1–0)$ for $C^{17}O$. It is equal to T_{kin} at high densities, but for about $5 \times 10^3 < n(H_2) < 5 \times 10^4$ cm^{-3} T_{ex} is larger than T_{kin}, while below 5 10^3 cm^{-3} this situation is reversed. The dashed and full-drawn lines indicate the difference in $T_{ex}(J = 1–0)$ between $C^{17}O$ and $C^{18}O$. $T_{ex}(C^{17}O)$ is larger than $T_{ex}(C^{18}O)$, in agreement with the observations (see Fig. 5g). For $T_{kin} < 20$ K the difference is less than 1 K. At low densities $T_{ex}(C^{18}O)$ is slightly larger than $T_{ex}(C^{17}O)$. In Fig. 9b the dotted lines show the difference in T_{ex} between the J = 2–1 and J = 1–0 transitions of $C^{17}O$. It is small for large $n(H_2)$ or low T_{kin}, but can reach values of more than 10 K for $T_{kin} > 20$ K and n(H_2) about 10^4 cm^{-3}. However the difference of this non-LTE effect between $C^{17}O$ and $C^{18}O$ (the full-drawn lines in Fig. 9b) is much smaller: about 1 K or less in the region where most data points are located in Fig. 8. Also these results are insensitive to changes in the assumed ortho/para H_2 ratio: larger changes in the excitation temperatures occur at higher temperatures ($T_{kin} > 25$ K) and lower densities ($n(H_2) < 10^4$ cm^{-3}) than those in the ρ Oph region. This suggests that while LTE calculations will overestimate column densities both for $C^{17}O$ and $C^{18}O$, the ratio of both column densities will be affected much less.

5. Discussion

In calculating the isotope ratios we did not distinguish between the different velocity components in the cloud (with typical velocity differences of about 2 kms^{-1}). The reason is the non-Gaussian line shape of many components which are confused by the hyperfine structure of $C^{17}O$ (3 components for J = 1–0 and 9 components for J = 2–1). Assuming a depth along the line of sight of 0.4 pc (10′), the crossing time for a velocity of 2 kms^{-1} would be 2.0×10^5 yr, which is probably much less than the lifetime of the cloud. This is at least 5.5×10^6 yr, the

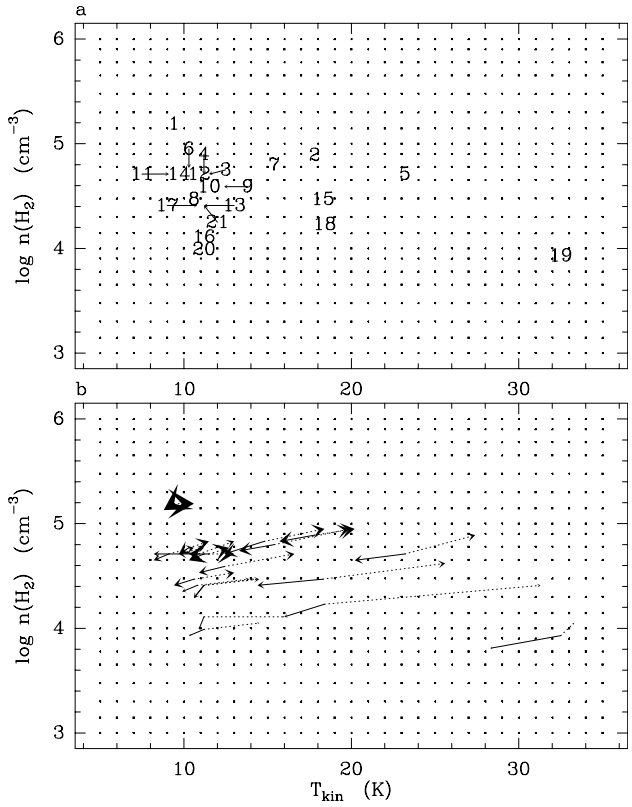

Fig. 8. a) Results of LVG calculations. For each of the 21 positions $T_{\rm kin}$ and $\log(n(\rm H_2))$ are given for the minimum χ^2 displayed in Fig. 7. **b**) The arrows show how $T_{\rm kin}$ and $\log(n(\rm H_2))$ change if $T_{\rm A}^*$ (full-drawn arrows) and $T_{\rm mb}^*$ (dotted arrows) are used. The sizes of the arrowheads are proportional to $\int T_{\rm A}^*[\rm C^{17}O(1–0)]dv$. In both panels the grid of dots indicate the $T_{\rm kin}$ and $n(\rm H_2)$ values used for the model calculations.

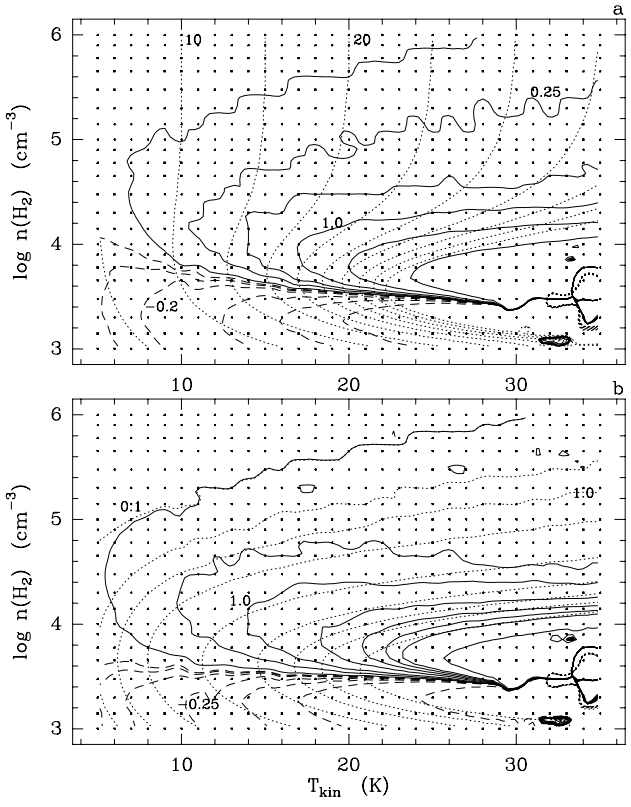

Fig. 9. A comparison of the $T_{\rm ex}$ of $C^{17}O$ and $C^{18}O$ derived from LVG model calculations. The grid of dots indicates the $T_{\rm kin}$ and $n(\rm H_2)$ values used for these calculations. **a**) The dotted lines indicate the non-LTE $T_{\rm ex}$ for $C^{17}O(1–0)$ derived from the LVG calculations using $C^{18}O/C^{17}O = 4.0$. Contour levels are (left to right) 5 to 50 K in steps of 5 K. The dashed and full-drawn lines show the difference in $T_{\rm ex}$ for the J=1−0 transition between $C^{17}O$ and $C^{18}O$: $T_{\rm ex}(C^{17}O) - T_{\rm ex}(C^{18}O)$. Contour levels are –2, –1, –0.5, –0.2, –0.1, –0.05 K (dashed), 0.025, 0.25, 0.5, 1, 2, 5, 10 K. Some contour values are labelled. **b**) The dotted lines show the difference in the non-LTE $T_{\rm ex}$ for two transitions of $C^{17}O$: $T_{\rm ex}[C^{17}O(J$=1−0)]–$T_{\rm ex}[C^{17}O(J$ = 2–1)]. Contour levels are (left to right) 0.1, 0.5, 1, 2, 5, 10, 15, 20, 30 K. The dashed and full-drawn lines compare the differences in non-LTE $T_{\rm ex}$ for $C^{17}O$ and $C^{18}O$: $(T_{\rm ex}[C^{17}O(J$ = 1−0)]–$T_{\rm ex}[C^{17}O(J$ = 2–1)]) – $(T_{\rm ex}[C^{18}O(J$ = 1)]–$T_{\rm ex}[C^{18}O(J$ = 2)]). Contour levels are –5, –1, –0.5, –0.25, –0.1, –0.05, –0.025 (dashed), 0.1, 0.5, 1, 2, 3, 4, 5, 10 K.

age of the Upper Scorpius subgroup of the Scorpius-Centaurus OB association (de Geus et al. 1989). Wilking et al. (1989) obtained an upper limit for the ages of the T Tauri stars in ρ Oph of 3.0×10^6 yr. This would provide enough time for sufficient mixing of the isotopic constituents of the gas. In addition the types of stars which produce ^{17}O and ^{18}O are not (yet) present in the ρ Oph cloud (they do exist in the nearby Upper Scorpius subgroup of the older Scorpius-Centaurus association), so both isotopes are not locally produced and it is unlikely that they are enhanced in some parts of the cloud by this mechanism (see e.g. Henkel & Mauerberger 1993). It also seems unlikely that stellar winds from these associations can alter the composition of the cloud significantly.

The results for the $C^{18}O/C^{17}O$ ratios are summarized in Table 5, with the transition and the method used.

The first three entries in Table 5 indicate that the observed ratio is very dependent on the transition used. We note that Penzias (1981) corrected his ratios only for the difference in frequency and not for optical depth effects. This suggests that also the J = 1–0 ratios used in Penzias' (1981) galactic study need some more analysis. This will be discussed in more detail together with new measurements in a forthcoming paper. Within the uncertainties the average J = 1–0 value is equal to the number obtained by Penzias (1981) for the galactic plane, 3.65 ± 0.15. The weighted average ratio of our LTE ratios is 4.17 ± 0.26, whereas the LVG calculations resulted in a ratio of 4.11 ± 0.14. Because this method combines all observational data we consider this the best result. Bensch et al. (2001) detected the almost certainly optically thin transitions $^{13}C^{18}O$ and $^{13}C^{17}O(1–0)$ towards pos. 1. Their observed $^{13}C^{18}O/^{13}C^{17}O$ ratio, corrected for the frequency difference is 4.23 ± 0.53. Using escape probability models they derived a ratio $^{18}O/^{17}O$ of 4.15 ± 0.52, which is identical to (but with a relatively large uncertainty because only one position was observed) the presently derived average value. Note that the position used by Bensch et al. (2001) had to be omitted from our calculations because of an undetermined optical depth.

Recently Ladd (2004) observed $C^{18}O$ and $C^{17}O(1–0)$ towards some 600 positions in the Taurus clouds and derives a ratio of 4.0±0.5, in agreement with the present result. However, the $C^{18}O/C^{17}O$ ratio appears to decrease with increasing

Table 5. Derived $C^{18}O/C^{17}O$ ratios compared with some previous results.

Ratio $C^{18}O/C^{17}O$	Trans.	Method	Omit pos.
3.53 ± 0.11	J = 1–0	freq. corr.	1
3.06 ± 0.11	J = 2–1	freq. corr.	1
2.78 ± 0.18	J = 3–2	freq. corr.	1
4.07 ± 0.32	J = 1–0	from $N_{\rm lte}$	1, 3, 4, 6
4.35 ± 0.44	J = 2–1	from $N_{\rm lte}$	1, 2, 3, 4, 6, 7, 9, 11
4.17 ± 0.26	average of J = 1–0 and 2–1	from $N_{\rm lte}$	
4.11 ± 0.14	J = 1–0, 2–1, 3–2; from LVG		
3.65 ± 0.15	J=1−0	Penzias (1981) gal. disk Freq. corr.	
4.15 ± 0.52	J=1−0	Bensch et al. (2001) From $^{13}C^{18}O/^{13}C^{17}O$ From exc. model	
4.23 ± 0.53	J=1−0	Bensch et al. (2001) From $^{13}C^{18}O/^{13}C^{17}O$ Freq. corr.	

integrated $C^{17}O$(1−0) intensity. Ladd then concludes that the ratio in the inner parts is 2.8 ± 0.4, due to larger self shielding of $C^{18}O$ in the outer parts. The range of integrated $C^{17}O$(1–0) intensity in Taurus (0.2 to 0.6 K km s^{-1}) is much smaller than in ρ Oph because of the smaller line widths. We think that this ratio of 2.8 is not real: our LVG models (using a smaller velocity gradient of 2.0 km s^{-1} pc^{-1} and an intrinsic $C^{18}O/C^{17}O$ ratio of 4.0) can reproduce the decrease in ratio with $I(C^{17}O)$ if positions with lower $I(C^{17}O)$ have a lower density and maybe kinetic temperature than the points with higher $I(C^{17}O)$, which is quite possible. In addition, it appears that when self-shielding is significant for $C^{18}O$, at $N(H_2) > 1.22\ 10^{21}$ (Frerking et al. 1982), or $A_v > 1.3$ mag (Bohlin et al. 1978), this corresponds to a far-UV extinction by dust of >13 mag (Aannestad & Purcell 1973). This implies that beyond this extinction (the $(C^{17}O)$ self-shielding H_2 column density is even higher) there is too little UV radiation left to affect the $C^{18}O/C^{17}O$ ratio, in contradiction with the suggestion by Ladd (2004). In ρ Oph a systematic decrease of $C^{18}O/C^{17}O$ with $I(C^{17}O)$ is not seen (see Fig. 4), except towards pos. 1.

6. Summary

From observations of up to three transitions of $C^{18}O$ and $C^{17}O$ towards 21 positions in the ρ Oph cloud we derive from LTE and LVG calculations $C^{18}O/C^{17}O$ abundance ratios of 4.17 ± 0.26 and 4.11±0.1, respectively. These are expected to be identical to the $^{18}O/^{17}O$ isotope ratio. The average molecular hydrogen density increases from about 10^4 cm^{-3} towards positions with low column densities to 10^5 cm^{-3} towards positions in the cloud cores. The kinetic temperatures decrease from 30 K or more at the edge of the cloud (as derived from the excitation temperatures of ^{12}CO) to 20 K at positions with weak $C^{17}O$ emission to 10 K in the cloud cores.

Acknowledgements. This work was supported in part by the Deutsche Forschungsgemeinschaft through grant SFB-494. The James Clerk Maxwell Telescope is operated by The Joint Astronomy Centre on behalf of the Particle Physics and Astronomy Research Council of the UK, the Netherlands Organisation for Scientific Research, and the National Research Council of Canada. We thank Carsten Kramer for his comments on an earlier version of this paper.

References

Aannestad, P. A., & Purcell E. M. 1973, ARA&A, 11, 309
Anders, E., & Grevesse, N. 1989, Geochim. Cosmochim. Acta 53, 197
Bally, J., & Langer, W. D. 1982, ApJ, 255, 143
Bensch, F., Pak, I., Wouterloot, J. G. A., Klapper, G., & Winnewisser, G. 2001, ApJ, 562, L185
Bergin, E. A., Alves, J., Huard, T., & Lada, C. J. 2002, ApJ, 570, L101
Bohlin, R.C., Savage, B. D., & Drake, J. F. 1978, ApJ, 224, 132
Castets, A., Duvert, G., Dutrey, A., et al. 1990, A&A, 234, 469
Castor, J. I. 1970, MNRAS, 149, 111
de Geus, E. J., de Zeeuw, P. T., & Lub, J. 1989, A&A, 216, 44
Flower, D. R. 2001, J. Phys. B: At. Mol. Opt. Phys., 34, 1
Frerking, M. A., Langer, W. D., & Wilson, R. W. 1982, ApJ, 262, 590
Harrison, A., Henkel, C., & Russell, A. 1999, MNRAS, 303, 157
Heikkilä, A., Johanssson, L. E. B., & Olofsson, H. 1998, A&A, 332, 493
Henkel, C., & Mauersberger, R. 1993, A&A, 274, 730
Isobe, T., Feigelson, E. D., Akritas, M. G., & Babu, G. J. 1990, ApJ, 364, 104
Kramer, C., Alves, J., Lada, C. J., et al., 1999, A&A, 342, 257
Ladd, E. F. 2004, ApJ, 610, 320
Langer, W. D., Graedel, T. E., Frerking, M. A., & Armentrout, P. B. 1984, ApJ, 277, 581
Langer, W. D., Wilson, R. W., Goldsmith, P. F., & Beichman, C. A. 1989, ApJ, 337, 355
Linke, R. A., Goldsmith, P. F., Wannier, P. G., Wilson R. W., & Penzias, A. A. 1977, ApJ, 214, 50
Loren, R. B., Wootten, A., & Wilking, B. A. 1990, ApJ, 365, 269
Lovas, F. J., & Krupenie, P. H. 1974, J. Phys. Chem. Ref. Data, 3, 245
Martin-Pintado, J., Wilson, T. L., Gardner, F. F., & Henkel C. 1983, A&A, 117, 145
Motte, F., André, P., & Neri, R. 1998, A&A, 336, 150
Penzias, A. A. 1981, ApJ, 249, 518
Prantzos, N., Aubert, O., & Audouze, J. 1996, A&A, 309, 760
Rohlfs, K., & Wilson, T. L. 1996, Tools of Radio Astronomy (Berlin: Springer-Verlag)
Scoville, N. Z., & Solomon, P. M. 1974, ApJ, 187, L67
van Dishoeck, E. F., & Black J. H. 1988, ApJ, 334, 771
Wang, M., Henkel, C., Chin, Y.-N., et al. 2004, A&A, 422, 883
Wilking, B. A., & Lada, C. J. 1983, ApJ, 274, 698
Wilking, B. A., Lada, C. J., & Young, E. T. 1989, ApJ, 340, 823
Wilson, T. L., & Rood, R. T. 1994, ARA&A, 32, 191
Zeng, Q., Batrla, W., & Wilson, T. L. 1984, A&A, 141, 127
Zielinsky, M., Stutzki, J., & Störzer, H. 2000, A&A, 358, 723